AGU PUBLICATIONS

Space Weather

RESEARCH ARTICLE
10.1002/2017SW001701

Key Points:
- Detection of a coronal mass ejection by estimation of the phase fluctuations in a spacecraft radio signal
- Use of VLBI radio telescope to characterize the propagation of spacecraft radio signals along the solar wind

Correspondence to:
G. Molera Calvés,
guifre.moleracalves@nls.fi

Citation:
Molera Calvés, G., Kallio, E., Cimo, G., Quick, J., Duev, D. A., Bocanegra Bahamón, T., … Mikhailov, A. (2017). Analysis of an interplanetary coronal mass ejection by a spacecraft radio signal: A case study. *Space Weather*, *15*, 1523–1534. https://doi.org/10.1002/2017SW001701

Received 23 OCT 2016
Accepted 23 OCT 2017
Accepted article online 13 NOV 2017
Published online 16 NOV 2017

Analysis of an Interplanetary Coronal Mass Ejection by a Spacecraft Radio Signal: A Case Study

G. Molera Calvés[1,2,3], E. Kallio[2], G. Cimo[3,4], J. Quick[5], D. A. Duev[3,6], T. Bocanegra Bahamón[3,7,8], M. Nickola[5], M. A. Kharinov[9], and A. G. Mikhailov[9]

[1]Finnish Geospatial Research Institute, National Land Survey of Finland, Helsinki, Finland, [2]School of Electrical Engineering, Department of Electronics and Nanoengineering, Aalto University, Espoo, Finland, [3]Joint Institute for VLBI ERIC, Dwingeloo, Netherlands, [4]ASTRON, The Netherlands Institute for Radio Astronomy, Dwingeloo, Netherlands, [5]Hartebeesthoek Radio Astronomy Observatory, Krugersdorp, South Africa, [6]California Institute of Technology, Pasadena, CA, USA, [7]Department of Astrodynamics and Space Missions, Delft University of Technology, Delft, Netherlands, [8]Shanghai Astronomical Observatory, Chinese Academy of Sciences, Shanghai, China, [9]Institute of Applied Astronomy of Russian Academy of Sciences, St. Petersburg, Russia

Abstract Tracking radio communication signals from planetary spacecraft with ground-based telescopes offers the possibility to study the electron density and the interplanetary scintillation of the solar wind. Observations of the telemetry link of planetary spacecraft have been conducted regularly with ground antennae from the European Very Long Baseline Interferometry Network, aiming to study the propagation of radio signals in the solar wind at different solar elongations and distances from the Sun. We have analyzed the Mars Express spacecraft radio signal phase fluctuations while, based on a 3-D heliosphere plasma simulation, an interplanetary coronal mass ejection (ICME) crossed the radio path during one of our observations on 6 April 2015. Our measurements showed that the phase scintillation indices increased by a factor of 4 during the passage of the ICME. The method presented here confirms that the phase scintillation technique based on spacecraft signals provides information of the properties and propagation of the ICMEs in the heliosphere.

1. Introduction

Interplanetary coronal mass ejections (ICMEs) are a manifestation of active processes in the Sun where a substantial amount of matter is released from the outer atmosphere as coronal mass ejections (CMEs) (Chen, 2011) to the heliosphere. These large-scale magnetic structures (Cane & Richardson, 2003; Gosling, 1990) are one of the most important space weather phenomena as they can cause large geomagnetic storms on Earth. An extreme Earth-directed ICME is also a potential hazard for man-made devices, such as satellites, communication lines, or power grids. Characterizing the properties of ICMEs is therefore a very important field of research in heliospheric and magnetospheric physics, and in space physics in particular.

Measuring the properties of ICMEs in situ is, however, difficult because this would require multiple spacecraft around the heliosphere. For this reason, it is of interest to look for remote sensing methods for characterizing ICMEs, such as the coronagraphs in the missions of the Solar and Heliospheric Observatory (Domingo et al., 1995) and the Solar Terrestrial Relations Observatory (Kaiser et al., 2008). However, remote observations have further limitations since ICMEs are often observed to be strongly deflected in both longitude and latitude as they depart from the corona (Kay et al., 2015). This complicates the estimation of whether an ICME would hit the Earth.

The amplitude and phase of any natural or man-made signal are disturbed when crossing an ICME. Natural radio sources have, for several decades, provided a tool to investigate heliospheric plasma by measuring interplanetary scintillation (see, e.g., Hewish et al., 1964; Jackson et al., 1998; Kojima et al., 1998), by comparing radio observations with solar and heliospheric images (see, e.g., Dorrian et al., 2008; Hardwick et al., 2013; Jones et al., 2007), by in situ solar wind observations (see, e.g., Coles et al., 1978), and by simulating the plasma of the heliosphere (see, e.g., Kim et al., 2014; Sokól et al., 2013).

Measurements of phase scintillation using radio signals of human origin transmitted by a spacecraft provide an additional tool to measure solar corona, heliosphere plasma, CMEs, and ICMEs by radio tracking techniques at ground stations (see, e.g., Bird et al., 1994, 1996; Duev et al., 2016; Karl et al., 1997; Molera Calvés, 2012; Pätzold et al., 2012).

Observations of planetary spacecraft have been carried out systematically since 2009 by the Planetary Radio Interferometry and Doppler Experiment (PRIDE) team by means of Very Long Baseline Interferometry (VLBI) instrumentation on ground radio telescopes (Duev et al., 2012; Molera Calvés, 2012). The propagation of the radio signal in the interplanetary medium has been used to estimate the electron density fluctuations in the solar wind (Molera Calvés et al., 2014). The campaign focused on tracking ESA's Venus Express (VEX) spacecraft from 2009 to 2014 (until mission termination), ESA's Mars Express (MEX) spacecraft, from the beginning of 2014 onward, and ESA's Rosetta comet spacecraft, from the beginning of 2015 to 2016 (until mission termination).

This study presents the analysis of variations in the radio communications signal transmitted by the MEX spacecraft in April 2015 as it propagated through the interplanetary plasma during the passage of an ICME across the line of sight. The method presented is sensitive to changes in the total electron column (TEC) density between the spacecraft and the Earth caused by the ICME. Electron density fluctuations can be used to characterize the properties of the ICME, such as size, structure, intensity, and propagation speed.

The paper is organized as follows: first, the technique used to process the spacecraft signals is introduced in detail in section 2.2. Second, the analysis of the data that led us to detect an ICME on the line of sight is described in section 2.3. After that follows a description in section 3 of how to characterize the properties of the ICME using data observed from two radio telescopes. Finally, the capability of a network of radio antennae to monitor similar events in the near future is discussed in section 4.

2. Method and Observations

2.1. Theory

The TEC between the spacecraft target and the Earth is defined as the integral of the electron density along the line of sight

$$\mathrm{TEC} = \int_{\mathrm{Earth}}^{\mathrm{spacecraft}} n_e(R) \cdot \mathrm{d}l, \tag{1}$$

where $n_e(R)$ is the electron density, which depends on the distance from the Sun (R). Several studies can be found in the literature about the estimation of the electron density along the line of sight. In this research, we have used the electron density model for a *slow* solar wind as described in You et al. (2012). In the paper we assign TEC_n as the TEC calculation based on You's density model.

The analysis of spacecraft radio signals allows one to determine the variation of the phase of a radio signal that is related to the variations in the electron density (δn_e) (see more in section 2.2). In Molera Calvés et al. (2014), we presented a study based on observations of Venus Express with VLBI radio telescopes. In that paper we established, as stated in previous studies (Coles et al., 1978; Woo et al., 1976, 1995), that the *phase scintillation index* (σ_{Sc}) is approximately proportional to the interplanetary plasma TEC

$$\mathrm{TEC} \propto \sigma_{\mathrm{Sc}}, \tag{2}$$

where σ_{Sc} is a measure of the level of fluctuations in the phase of the spacecraft signal caused by the propagation in a turbulent media. The σ_{Sc} is defined as the standard deviation of the measured phase of the signal. The PRIDE group has conducted hundreds of observations since 2009 to establish a relationship between the TEC and the phase scintillation index at any given solar elongation. This relationship is summarized by the expression (Molera Calvés, 2012)

$$\mathrm{TEC}_{\sigma_{\mathrm{Sc}}} = 2 \cdot K_s \cdot \sigma_{\mathrm{Sc}} \cdot \left(\frac{f_{\mathrm{obs}}}{8.4\mathrm{GHz}}\right) \cdot \left(\frac{300\mathrm{s}}{\tau}\right)^{\frac{m+1}{2}}, \tag{3}$$

where $\mathrm{TEC}_{\sigma_{\mathrm{Sc}}}$ is expressed in total electron content units ($1\mathrm{TECU} = 10^{16}$ electrons/m^2). The parameter K_s (TECU/rad) is an empirically determined constant based on observational data from spacecraft. These hundreds

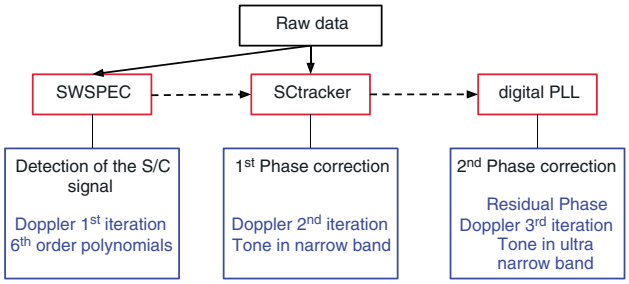

Figure 1. Illustration of the data analysis steps and software modules used for spacecraft tracking purposes: SWSpec, SCtracker, and digital phase-locked loop. All the software is developed and maintained jointly by the Joint Institute for VLBI ERIC and Aalto University.

of observations have yielded to obtain one value for K_s with data from VEX and another one with data from MEX. They are based on several hundreds of observations conducted over 8 years. Thus, they cover all conditions of slow and fast winds, as well as a wide range of solar elongations and Earth-spacecraft distances (Molera Calvés et al., 2014). Continuing in equation (3), f_{obs} is the communication frequency of the spacecraft (GHz), which usually lies between 8.30 and 8.50 GHz, τ is the integration time [s] (typically τ is 300 s), m is the spectral index (based on the observations by Molera Calvés et al. (2014)), m is approximately −8/3, which is consistent with a Kolmogorov power spectrum of fluctuations (Kolmogorov, 1991), and σ_{Sc} is the phase scintillation index (rad) retrieved from the observations conducted by the radio telescopes. f_{obs}, τ, and m allow us to adjust the equation depending on the spacecraft and the measurement results. However, in the standard VEX or MEX observations those terms cancel themselves out. A factor of 2 is included to take into account the two-way link between the Earth and the spacecraft. In this paper we refer to $TEC_{\sigma_{Sc}}$ as the TEC derived from the phase scintillation index as per equation 3.

2.2. Processing of the Radio Signal

The setup of our observations is known as *three-way* radio link, where the radio signal transmitted by a spacecraft to a ground station telescope is tracked by a secondary radio telescope (Asmar et al., 2005). The spacecraft and the ground station operate in the so-called *two-way* mode, where the ground telescope transmits a signal to the spacecraft and receives it back. Meanwhile, the second telescope detects the signal and compares it to a locally generated frequency. The VLBI radio telescopes use independent hydrogen masers as their reference clock.

Sessions are planned accordingly to the transmission schedule provided by the mission support team. The antenna schedules are then prepared for the available telescopes. Data are recorded locally at the telescope and transferred offline to the processing center, minutes after the end of the session. The data processing is conducted at the Joint Institute for VLBI ERIC (Dwingeloo, The Netherlands) and at the Aalto University Metsähovi Radio Observatory (Espoo, Finland).

The narrowband data processing of the single dish open-loop data collected by the radio telescopes is divided into three blocks, as shown in Figure 1: the SWSpec, SCTracker, and digital PLL software (https://github.com/gofrito/swspec) (Molera Calvés, 2012).

SWSpec extracts the raw data from the channel where the spacecraft carrier tone is recorded, and then it performs a window-overlapped add (WOLA) discrete Fourier transform (DFT) and an integration over the obtained spectra. The result is an initial estimate of the spacecraft carrier tone Doppler residual along the scan. The moving phase of the carrier tone throughout the scan is modeled by performing an n-order frequency polynomial fit. We have fitted the data with a polynomial of order 6 through the entire research. SCtracker uses this initial fit to stop the phase of the carrier tone, allowing subsequent tracking, filtering, and extraction of the carrier tone in a narrower band (from the initial 16 MHz channel bandwidth down to a 2 kHz bandwidth), using a second-order WOLA DFT-based algorithm of the Hilbert transform approximation. The digital phase-locked loop (dPLL) performs high-precision iterations of the previous steps—time integration of the overlapped spectra, phase polynomial fitting, and phase-stopping correction—on the 2 kHz bandwidth signal. The output of the dPLL is the filtered and down-converted signal, and the residual phase in the stopped band with respect to the initial phase polynomial fit. The bandwidth of the output detections is 20 Hz with a frequency spectral resolution of 2 mHz. The Doppler residual is obtained by adding the base frequency of the selected channel to the 10 s averaged carrier tone frequencies after the dPLL. For more details see Molera Calvés et al. (2014).

The outputs of this analysis are the fluctuations of the recorded Doppler residual and the residual phase variations of the signal for the particular line of sight (Earth-spacecraft) in intervals of 20 min. The accuracy of the detections of the Doppler residual and the fluctuations in the signal phase allows us to extrapolate the electron density variations.

Table 1
Summary of the Observations Conducted of MEX in April 2015

Epoch	Station	No. of scans	Weather condition	Ground station	Start observation	Stop Observation	Azimuth	Elevation
2015.04.03	Ht	3	Cloudy	NNO	14:20	15:20	304° – 297°	30° – 22°
2015.04.04	Ht	3	Rainy	NNO	14:20	15:20	304° – 297°	30° – 22°
2015.04.06	Ht	4	Clear	CEB	07:20	08:40	65° – 52°	22° – 33°
2015.04.06	Bd	10	Clear	CEB	05:20	08:40	160° – 225°	50° – 43°
2015.04.09	Bd	14	Rainy	CEB	03:00	07:40	160° – 250°	50° – 33°

Note. Columns from left to right give the epoch (day.month.year), observing station (Ht, Hartebeesthoek and Bd, Badary), number of scans, weather conditions at the site, ESA's ground station (NNO, New Norcia, Australia and CEB, Cebreros, Spain), initial and ending time of the observations (in UTC), ranges of the azimuths, and elevations tracked by the telescopes.

2.3. Radio Observations

In April 2015, three consecutive sessions targeting MEX were conducted with the same radio telescope, the 15 m antenna at the Hartebeesthoek radio astronomy observatory (Ht, South Africa). These observations were carried out under different weather conditions: the first day under heavy clouds, the second with strong wind and rain, and the last with clear sky. As described in Molera Calvés et al. (2014), the atmospheric conditions have little influence on the results. The results indicated that the worst measurement in terms of detection accuracy of the spacecraft signal was achieved with clear sky, on 6 April 2015.

This session consisted of tracking the MEX signal with the South African antenna and the Badary 32 m radio telescope (Bd, Russia). Hence, we decided to investigate further what might have occurred during this session. Badary observed MEX from 05:00 to 08:40, while Ht observed from 07:20 to 08:40. So, there were overlapping observations for 80 min (four scans). The summary of the observations conducted around the vicinity of 6 April 2015 is shown in Table 1.

Badary's observation yielded similar results to those at Hartebeesthoek, being namely the phase scintillation higher than in standard conditions. The matching of results between both radio telescopes suggested that a plasma anomaly, later identified as an ICME, may have been detected.

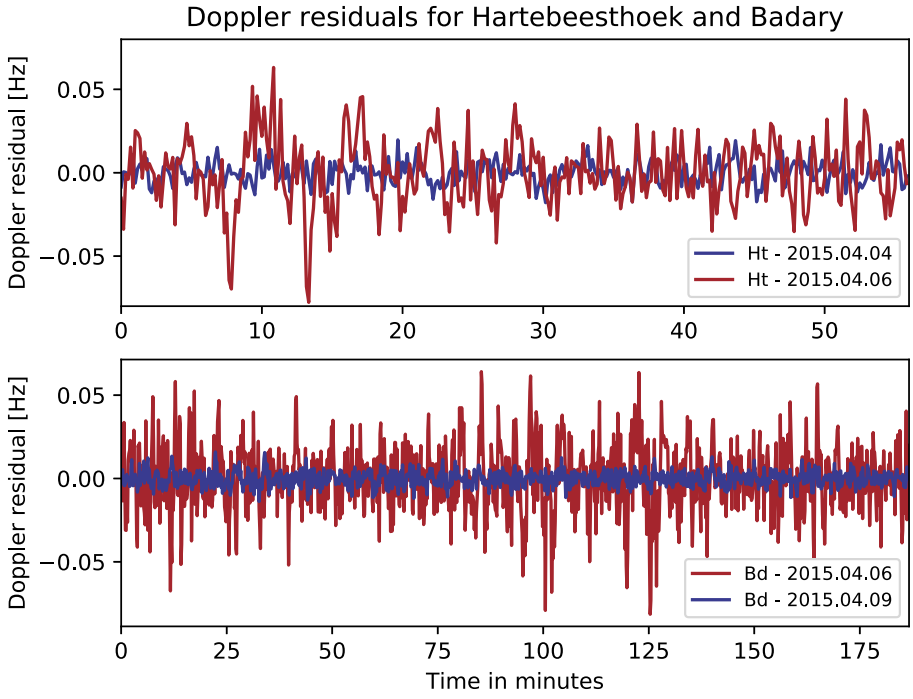

Figure 2. Doppler residuals detected at the radio telescopes of (top) Hartebeesthoek and (bottom) Badary comparing data observed during the days around the ICME. Data during the ICME on 6 April 2015 are shown in red. Data observed on 4 and 9 April 2015 are in blue. The initial time on the graph corresponds to the start of the observation, as specified in Table 1.

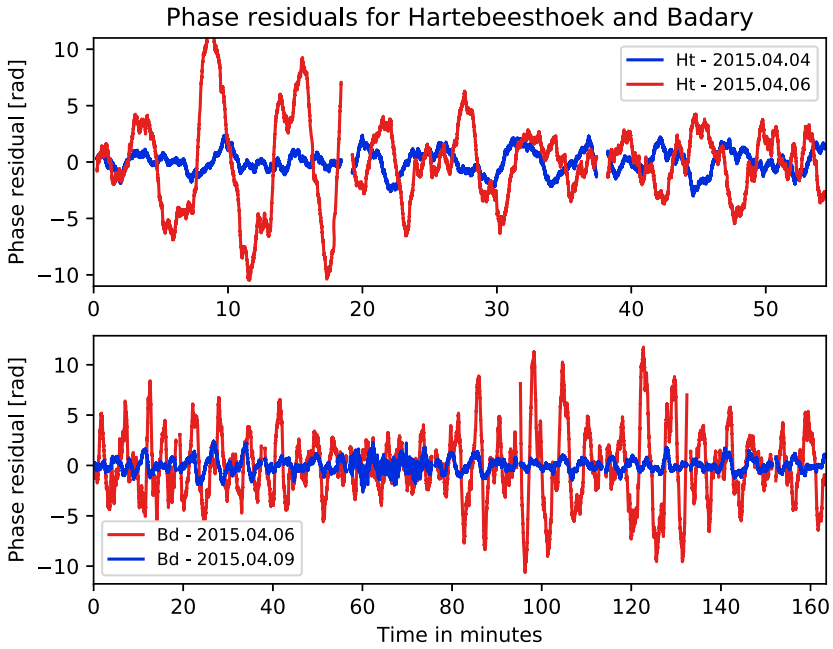

Figure 3. Phase residuals extracted from the radio telescope at (top) Hartebeesthoek and (bottom) Badary data observed during the days around the ICME. Data during the ICME on 6 April 2015 are shown in red. Data observed on 4 and 9 April 2015 are in blue. The initial time on the graph corresponds to the start of the observation, as specified in Table 1.

Figure 2 compares the detection in frequency terms of the MEX radio signal before, during, and after the ICME. Figure 2 (top) shows the Doppler residual of the full session observed on 4 April 2015 (blue line) and 6 April 2015 (red line) at the Hartebeesthoek station. Figure 2 (bottom) shows the residuals measured on 6 (red line) and 9 (blue line) April 2015 at the Badary telescope. It is clear from Figure 2 that the fluctuations of the Doppler residuals are much higher for the analyzed ICME than similar measurements collected in its vicinity.

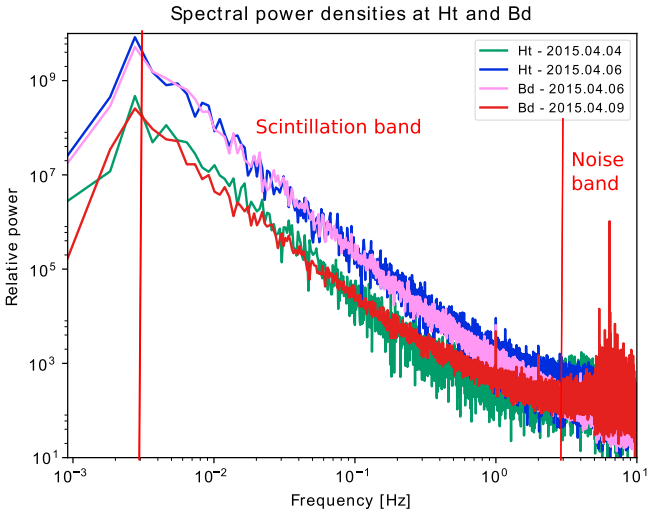

Figure 4. Comparison of the spectral power density of the phase fluctuations for sessions with the Hartebeesthoek (Ht) antenna on 4 (green line) and 6 (blue line) April 2015, and with the Badary (Bd) antenna on 6 (violet line) and 9 (red line) April 2015. Note that the spectral signature of the ICME has a relative power 2 orders of magnitude above the nominal solar wind conditions at similar solar elongations.

The drastic change on the behavior of the radio signal during the ICME can be better seen in the plot of the residual phase of the signal. Figure 3 shows the residual phase measured at Hartebeesthoek (top) on 4 April 2015 (blue line) and 6 April 2015 (red line), and at Badary (bottom) on 6 April 2015 (red line) and 9 April 2015 (blue line). Several scans during the ICME pass show phase fluctuations that are 10 times higher than during undisturbed solar wind conditions. The data provided on 9 April 2015 reflect nominal conditions, since the results are in good agreement with spacecraft data collected since 2009. For comparison, the initial time is assumed to be the same and the *x* axis shows the relative time with respect to the beginning of the sessions. The periodicity seen in the residual phase is a known feature due to the extraction method.

The spectral signature of the phase fluctuations is another valid way to look at the results. The level of the scintillation can be extrapolated by estimating the integral of the spectral power density of the phase fluctuations (Molera Calvés et al., 2014). The spectral power density of the phase fluctuations for sessions with Hartebeesthoek on 4 (green line) and 6 (blue line) April 2015, and with Badary on 6 (violet line) and 9 (red line) April 2015 are shown in Figure 4. The peaks of the power spectra in both sessions observed on 6 April 2015 are 2 orders of magnitude higher than in the other two.

The Doppler residuals, phase fluctuations, and spectral signature statistics for these observations are summarized in Table 2. For the estimates, we used the

Table 2
Measurements Obtained From Five Observations Around 6 April 2015

Epoch	Station	Doppler mean	Phase fluctuations	Spectral peak	σ_{Sc}	$TEC_{\sigma_{Sc}}$
2015.04.03	Ht	5.1 ± 0.8 mHz	0.51 ± 0.11 rad	230 rad^2/Hz	0.482 rad	964 TECU
2015.04.04	Ht	6.9 ± 0.4 mHz	0.65 ± 0.07 rad	1153 rad^2/Hz	0.558 rad	1116 TECU
2015.04.06	Ht	19.1 ± 3.8 mHz	1.96 ± 0.59 rad	17477 rad^2/Hz	1.537 rad	3074 TECU
2015.04.06	Bd	19.7 ± 4.0 mHz	2.25 ± 0.56 rad	12550 rad^2/Hz	2.170 rad	4340 TECU
2015.04.09	Bd	4.3 ± 0.6 mHz	0.44 ± 0.10 rad	763 rad^2/Hz	0.512 rad	1024 TECU

Note. The columns from the left to right are epoch, name of the station (Ht, Hartebeesthoek and Bd, Badary), Doppler residual average, phase fluctuations average, spectral peak, phase scintillation index (σ_{Sc}), and $TEC_{\sigma_{Sc}}$.

f_{obs} of MEX that is equal to 8.421 GHz, an integration time of 5 min, and the value of K_s empirically found by spacecraft observations collected from MEX data (from 2014 to 2016) (Molera Calvés et al., 2014). The K_s factor from over 450 observations on MEX is approximately 2010 TECU/rad.

3. Interpretation of the Observations

3.1. CME Simulations and In Situ Observations

CACTUS online software (http://sidc.oma.be/cactus/) registered a solar eruption produced on the surface of the Sun at 23:48 UTC on 4 April 2015. This solar eruption evolved into a flare of intensity of type C and with a coronal mass ejection. This CME (internal reference number: 0012) propagated with an angle of emission with respect to north of 115° and an angular width of 176°. The average speed of the ICME was 400 km/s, with a minimum and maximum velocity of 103 and 1,358 km/s. Further information about the ICME is available online at the Integrated Space Weather Analysis System (iSWA, http://iswa.gsfc.nasa.gov/).

The ICME propagated toward a latitude of −3° in the elliptic plane. According to the computer simulation, shown in Figure 5, almost 24 h later, at 00:00 UTC on 6 April 2015, the ICME crossed the line of sight (shown by a black arrow) between Mars (red circle) and Earth (yellow circle). The Badary radio telescope started the

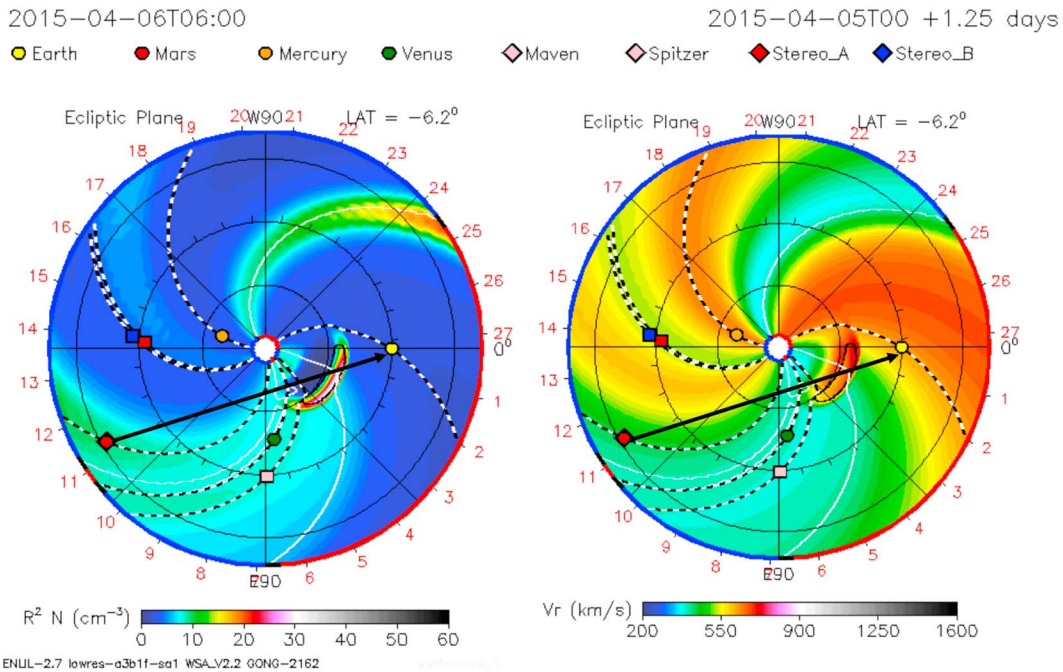

Figure 5. Geometrical configuration and plasma properties of the heliosphere when the ICME was at about 0.5 AU. (left) Electron density content times R^2 [$N(cm^{-3})$]. (right) Solar wind radial speed on the elliptic plane in km/s. The simulation is for the time of our observations (6 April 2015 at 06:00 UTC). A black arrow is added to show the line of sight from Mars (red circle) to the Earth (yellow circle). Simulations are available through the Integrated Space Weather Analysis System (iSWA, https://ccmc.gsfc.nasa.gov/iswa/).

Table 3
TEC Estimations Along the Line of Sight for the MEX Observations in April 2015: Epoch, Radio Telescopes (Ht, Hartebeesthoek and Bd, Badary), Ionospheric TEC for the Ionospheric Downlink (Ground Station Spacecraft) and the Uplink (Spacecraft Radio Telescope), and the Interplanetary Plasma Derived From You et al. for a Slow Wind Model (TEC_n)

Observation		Total electron content (in TECU)		
Epoch	Station	Ionospheric downlink	Ionospheric uplink	Solar wind
2015.04.03	Ht	95.9	103.1	1,299
2015.04.04	Ht	96.2	100.1	1,320
2015.04.06	Ht	71.9	59.8	1,357
2015.04.06	Bd	42.6	59.8	1,356
2015.04.09	Bd	48.3	57.0	1,423

observations at 05:00 UTC. The radio communications signal between Mars Express and the ground station of New Norcia crossed the ICME in both directions. At that time, Mars was at a solar elongation of 17.23° and a distance of 2.39 AU with respect to the Earth. Meanwhile, the ICME was at a distance of 0.5–0.6 AU from the Sun or at 1/5 of the path between the spacecraft and the observer, moving toward the latter.

Based on the computer simulation in Figure 5, we estimate that the radio signal intersected the plasma cloud with an approximate angle of incidence of 12°. The simulation covers the time of our observations (6 April 2015 at 06:00 UTC) when the ICME is present between Mars and Earth. The ENLIL simulations were prepared by the Community Coordinated Modelling Center at Goddard space center and are available through the Integrated Space Weather Analysis System (iSWA, https://ccmc.gsfc.nasa.gov/iswa/). The electron density and the radial speed of the solar wind in the ecliptic plane (as based on a computer simulation at the time of the observations) are presented in Figure 5 (left and right), respectively.

3.2. Interpretation of the Radio Observations

On 3–4 April 2015, the observations were carried out in the evening, when the spacecraft was locked to the ESA ground station in Malargüe (Argentina). The other data sets were collected in the morning, when the spacecraft was locked to the ESA ground station in New Norcia (Australia). The European Space Operations Centre (ESOC) confirmed that no data anomalies were encountered on the transmitting pipeline during the aforementioned days. Therefore, it was confirmed that the signal disturbance analyzed in this paper was not introduced during the transmission phase.

It was important to analyze how the different azimuth and elevation values affected the ionospheric and solar wind TEC contributions and, therefore, might have influenced our Doppler measurements. To estimate the contribution of the Earth's ionosphere, we used the vertical TEC (vTEC) maps provided by the International GSS Service (IGS) on the basis of postprocessing Global Navigation Satellite Systems (GNSS) (GPS and GLONASS) observations. The IGS fits the GNSS data to the single thin ionospheric layer model to estimate the vTEC values on a global grid with a spatial resolution of 5° in longitude and 2.5° in latitude and a 2 h temporal resolution. Detailed description of the ionospheric postprocessing can be found in Duev et al. (2012).

Next, we estimated the expected TEC contribution of the solar wind under undisrupted conditions. We used the approach described by You et al. (2012) that takes into account the electron density models for fast and slow solar winds. The two-way interplanetary plasma TEC is corrected for the uplink and downlink frequency ratio at X band by a factor of $1 + 880/749$ (Armstrong, 1998). Table 3 shows the TEC contribution for the ionosphere uplink (ground station spacecraft), and downlink (spacecraft VLBI radio telescope), and the solar wind (TEC_n).

As can be seen from Table 3, the ionospheric values were relatively steady during the observations: values varying between 40 and 100 TECU. Ionospheric TEC fluctuations are much smaller than changes seen in the solar wind TEC model. This also suggested that the fluctuations in our data were generated in space by some high-density plasma phenomena, such as an ICME, which moved through the line of sight and not by the ionosphere.

Once the detection of an ICME in the radio signal observed by our radio telescopes was verified as seen in section 3.1, we characterized and studied its properties. First, we analyzed the phase scintillation indices and Doppler measurements independently for each of the four scans observed at Hartebeesthoek and the

Table 4
Parameters for Each Scan on 6 April 2015 With Hartebeesthoek (Ht) and Badary (Bd) Radio Telescopes: Initial Time of the Scan, the Phase Scintillation Index (σ_{Sc} in rad), the Slope of the Spectral Power Density, the Spectral Peak (in rad^2/Hz) at 3 mHz, the Noise Level (in rad^2/Hz), the Doppler Accuracy (in Hz) and the Relative Signal-to-Noise Ratio

Time	Station	σ_{Sc}	Spectral slope	Spectral peak	Noise level	Doppler accuracy	SNR
05:20	Bd	2.568 ± 0.015	-2.828 ± 0.079	12,550	1.28×10^{-4}	23.36	82,471
05:40	Bd	2.014 ± 0.014	-2.828 ± 0.079	12,550	1.28×10^{-4}	17.16	84,111
06:00	Bd	2.179 ± 0.013	-2.828 ± 0.079	12,550	1.28×10^{-4}	15.16	87,518
06:20	Bd	1.328 ± 0.013	-2.828 ± 0.079	12,550	1.28×10^{-4}	14.93	88,385
06:40	Bd	3.013 ± 0.013	-2.828 ± 0.079	12,550	1.28×10^{-4}	20.65	88,059
07:00	Bd	2.836 ± 0.023	-2.828 ± 0.079	12,550	1.28×10^{-4}	25.16	90,772
07:20	Bd	3.053 ± 0.022	-2.828 ± 0.079	12,550	1.28×10^{-4}	26.05	87,260
07:40	Bd	1.847 ± 0.014	-2.828 ± 0.079	12,550	1.28×10^{-4}	16.02	85,675
08:00	Bd	1.995 ± 0.014	-2.828 ± 0.079	12,550	1.28×10^{-4}	19.42	84,859
08:20	Bd	1.654 ± 0.014	-2.828 ± 0.079	12,550	1.28×10^{-4}	15.51	79,284
07:20	Ht	2.983 ± 0.028	-2.744 ± 0.114	17,477	3.24×10^{-4}	25.43	24,603
07:40	Ht	1.750 ± 0.021	-2.744 ± 0.114	17,477	3.24×10^{-4}	16.22	25,394
08:00	Ht	1.537 ± 0.021	-2.744 ± 0.114	17,477	3.24×10^{-4}	16.97	25,914
08:20	Ht	1.604 ± 0.021	-2.744 ± 0.114	17,477	3.24×10^{-4}	16.41	26,632

10 scans observed at Badary. Table 4 presents the main statistics for all scans observed on 6 April 2015. The average σ_{Sc} from Hartebeesthoek and Badary data was 1.537 rad and 2.170 rad, respectively.

Table 4 shows the high variability of the results within the session. Both the Doppler accuracy and the phase scintillation index show a high standard deviation amongst the samples. In normal observations dispersion is common, however, not at the levels presented here. The spectral slope, the spectral peak, and the noise level are estimated using the spectral power plot (see Figure 4) and represent the average of all scans observed within one session.

The Doppler residuals, the σ_{Sc} measurement for 3 h of the session at both radio telescopes, are shown in Figure 6. Figure 6 (top) presents the measurements of Doppler accuracy for each 20 min scan. The data from

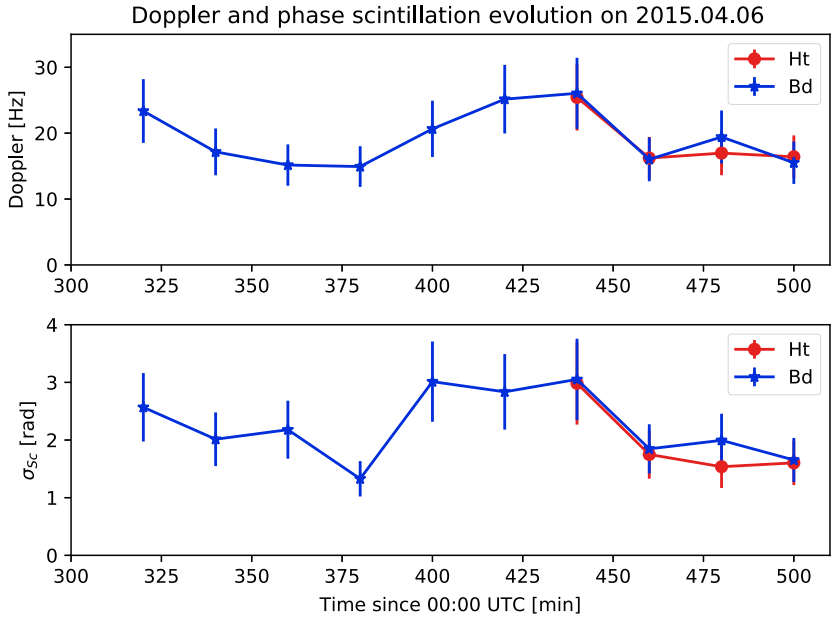

Figure 6. MEX data from 6 April 2015: (top) the variability of the Doppler detection and (bottom) the variability of the phase scintillation for the 3 h of observations. The data from the Badary (Bd) and Hartebeesthoek (Ht) stations are plotted in blue stars and red circles, respectively.

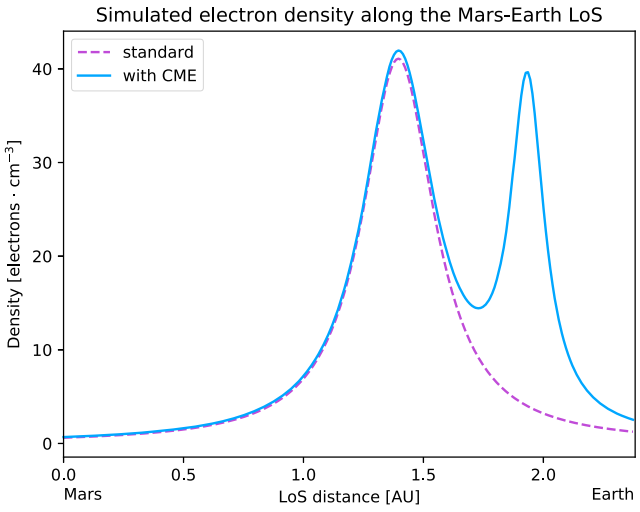

Figure 7. Electron density models of the solar wind between MEX and Earth on 6 April 2015, at 06:00 UTC. The two profiles are analytical fits of the electron density values along the line of sight from Mars to Earth for the TEC with and without the ICME. The dashed line shows the modeled electron density of the undisturbed solar wind (TEC = 1,350 TECU) and the solid line with the ICME (TEC = 1,950 TECU).

Badary are plotted with blue stars and from Hartebeesthoek in red circles. Measurements from Hartebeesthoek telescope are displaced because the antenna started observing 2 h later than Badary. Figure 6 (bottom) presents the measurements of the phase scintillation index using the same color scheme. As seen in the graphs, a similar feature is present on the data sets from both radio telescopes at the same time, eliminating a possible instrumental effect from the stations. The measurement errors have been included in both cases.

We estimated the expected TEC along the line of sight based on our measurements (defined as $TEC_{\sigma_{Sc}}$ from equation (3), using the data presented in Table 4. As the observations and the processing were conducted in our standard mode (i.e., $f_{obs} = 8.421$ GHz and $\tau = 300$ s) equation (3) gets the form

$$TEC_{\sigma_{Sc}} = 2 \cdot K_s \cdot \sigma_{Sc}, \tag{4}$$

where K_s is 2010 TECU/rad in the case of MEX data (as discussed in section 2.3) and the values of σ_{Sc} are given in Table 2. The average value of the σ_{Sc} measurements from all scans observed at Hartebeesthoek and Badary telescopes was 1.537 rad and 2.170 rad, respectively. Thus, the estimated $TEC_{\sigma_{Sc}}$ is equal to 3,430 TECU for Hartebeesthoek and 4,340 TECU for Badary. The expected TEC_n value based on You et al. (2012) model, as was shown in Table 3, was 1,357 TECU. We assumed that the measured TEC, which is 2.5 times higher in the case of Hartebeesthoek and 3.5 times in the case of Badary than the expected TEC values, is caused by the presence of the ICME along the line of sight.

3.3. ICME Density Profile

To evaluate the effect of the ICME on the spacecraft signal, we generated a 2-D model of the electron density/content along the line of sight. The model is based on two inputs: the simulation of the electron density estimated from the ENLIL simulation (Figure 5) and the electron density model from You et al. (2012) (Figure 7).

The dashed line in Figure 7 shows the electron density model of the undisturbed solar wind (TEC_n). The solid line shows the solar wind while adding the simulation of the ICME. In order to model the effect of the ICME, we have taken a 1-D section along the line of sight of the electron density map of Figure 5 (left) and reconstructed its smoothed density profile. The total electron content model including the ICME model is referred to in this paper as TEC_{nc}.

Table 5 compares the two simulations of the electron content model along the line of sight based on the measurements from the two radio telescopes. TEC_n is the undisturbed solar wind based on You et al. (2012) model, TEC_{nc} is the integral of the 2-D electron density profile with the ICME shown in Figure 7, and $TEC_{\sigma_{Sc}}$ is based on the data collected at each radio telescope.

The different TEC values between the models and the measurements obtained by the radio telescopes are probably related to the propagation and inner structure of the ICME. Studies have been carried out to examine their properties and explain their propagation in the heliosphere (Davis et al., 2009; Liu et al., 2008). These studies suggest that the ICME contains two components: a shockwave moving at high speed, dense plasma

Table 5
Estimated TEC Values Using Three Solar Wind Density Methods: (i) Undisturbed Solar Wind Contribution Based On You et al. (2012) Model (TEC_n), (ii) Integral of the 2-D Electron Profile Derived From the ICME Simulation in Figure 7 (TEC_{nc}), (iii) and Our Estimation Based On the Phase Scintillation Index and Equation (3) From Harteebesthoek (Ht) and Badary (Bd) Telescopes ($TEC_{\sigma_{Sc}}$)

Symbol	Definition	TEC
TEC_n	You et al. (2012) n_e model without the ICME	1,350 TECU
TEC_{nc}	electron profile with the ICME	1,950 TECU
$TEC_{\sigma_{Sc}}$ (Ht)	derived from σ_{Sc} Ht measurements	3,430 TECU
$TEC_{\sigma_{Sc}}$ (Bd)	derived from σ_{Sc} Bd measurements	4,350 TECU

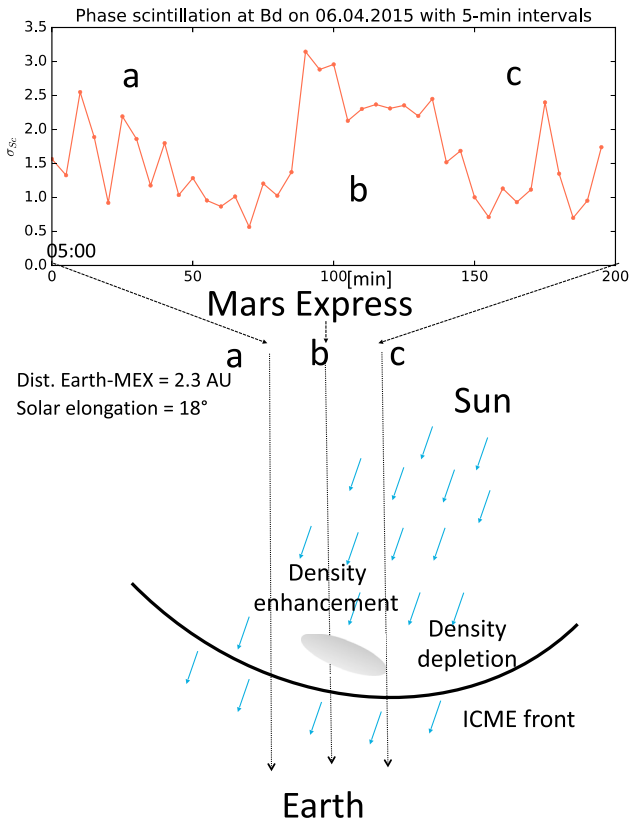

Figure 8. Sketch of the ICME based passing through the (bottom) Earth-Mars line and the phase variability during the full observation of MEX on 6 April 2015 at 5 min intervals, from 05:00 at the (top) Badary station. During the entire 180 min of observation the ICME was present in the line of sight. A density enhancement within the ICME was encountered during the middle of the observation, shown as region (b), lasting about 60 min.

density and tenuous magnetic field, and a cavity moving at lower speed, weak plasma density but stronger magnetic field. Our studies showed that the modeled TEC_{nc} is lower than the measured $TEC_{\sigma_{Sc}}$, which could be caused by different values of K_s in these two cases. Therefore, there is no guarantee that the average value of K_s, calculated for the general case (equation (3), is appropriate for ICMEs. How the K_s may differ in these two regions is not yet known. Furthermore, in Molera Calvés (2012) it was argued that 20 min of observational data was enough to characterize the outer scale of turbulences assuming typical speed of plasma inhomogeneties. However, due to the nature of the inner part of the ICME the scaling parameter K_s would be sensitive to velocity changes. Recently, Pätzold et al. (2012) studied the general structure of CMEs by using radio occultation measurements and compared it to the electron column density variations. In their model a large-scale density variation occurs only once in the sheath region of the CME, meanwhile a small density peak associated with the shock precedes the sheath region.

One natural question to ask is whether we can derive information about the inner structure of the ICME based on these observations. According to the ENLIL simulation (Figure 5), the velocity of the ICME is approximately of the order of 700 km/s. The total time span during which the radio signal crosses the large disturbance region inside of the ICME is about 50 min (see Figure 6). The distance traveled by the ICME during this period is therefore about 0.014 AU or about 10% of the size of the ICME as estimated from Figure 5. Figure 8 shows an illustration of a feasible simple model for the structure of this ICME.

We associate the first peak seen in the phase scintillation measurements at around 05:00 to the transit of the transmitted radio signal through the sheath of the ICME (a). The peak is immediately followed by a bump that we attribute to the signal propagating through the plasma cloud/density enhancement with very high density region (b). The electron column fluctuations reduce when the radio signal propagates only through the sheath of the ICME again (c).

We can speculate that the spacecraft signal has passed transversally through a plasma cloud with very high density inside the ICME between the shockwave and the tail, which drastically enhances the disturbance of the signal. Why this high density region would have resulted such a strong disturbance and how to quantify it is unclear. Unfortunately, we do not have enough information to associate this high density layer directly with the ICME's cloud. It is finally worth noting that the results of the frequency and phase variation analysis are similar to those presented recently by Pätzold et al. (2012) and Ando et al. (2015).

3.4. Cross Correlation of the Residual Phase

In addition to the analysis presented above, it should be possible, at least on a theoretical point of view, to derive more information on the ICME by cross correlating the residual phases. Following the work done by Efimov et al. (2008, 2009), we attempted to cross correlate the phase of the signal recorded at the two telescopes. Such a correlation would retrieve parameters of the time lag and plasma speed of the ICME. In our case, the telescopes observed simultaneously for the last four scans, that is, 80 min. The sampling time was 25 ms. The initial times for each of the four scans were different but were subsequently correctly realigned.

However, we did not succeed in correlating the residual phases. The distance between the telescopes was probably too large: 9,000 km north-south and 5,000 km east-west. This would require, for proper correlation, a strong extragalactic source as phase calibrator (Beasley & Conway, 1995). The use of such a source as phase reference will be considered in future observations.

4. Conclusions

This paper describes the detection of an interplanetary coronal mass ejections (ICME) using the two-way radio communications link between a planetary spacecraft and ground radio telescopes. Our technique measured

a phase scintillation index 3 times higher when crossing the ICME than during undisturbed solar wind conditions. Radio tracking is a valuable technique to study the properties of ICMEs with ground-based observations. In our study we calculated the TEC of the plasma anomaly, which is more than 3,000 TECU (see Table 5). Furthermore, we estimated using a simplified description the size of the internal structure of the ICME observed, which was to be around 0.014 AU. It is worth noticing that the probability of detection of an ICME is low: over the past 7 years and 500 observations only one such event has been detected.

In the future, using several spacecraft around the heliosphere, for example, small size CubeSatellites, it would be possible to make a 2-D or a 3-D tomography of the heliosphere by using the multiple lines of sight between the Earth and the satellites. However, even now, real-time observations of ICME events are possible, provided that there is a quick reaction to strong flare spots on the Sun, a suitable spacecraft-Earth-CME geometry and rapid coordination with a radio telescope. The use of radio telescopes that already monitor 24/7 for possible solar flares could allow real-time observations studying ICMEs and their propagation.

Future analysis of ICMEs could be improved in three ways: (i) by the use of more detailed modeling of the density within the ICME taking into account its 3-D motion and orientation; moreover, about 30% of the registered ICMEs contain also magnetic cloud-like structures (Cane & Richardson, 2003), and those 3-D structures could also be modeled; (ii) by addition of in situ ICME plasma or magnetic field measurements by a planetary spacecraft (see, e.g., Futaana et al., 2008; Kubicka et al., 2016) to remote sensing radio wave observations; and (iii) by conducting longer observations that cover the entirety of the pass of the ICME, it would be possible to measure precisely its effect before, during, and after the event.

Overall, this study suggests that spacecraft radio-link scintillation analysis can be used to detect ICMEs and to analyze their properties, especially, when the observations are integrated into global heliospheric models.

Acknowledgments
This work was made possible by observations conducted by a number of EVN radio telescopes. The EVN is a joint facility of European, Chinese, Russian, and South African institutes funded by their National Research Councils. The authors would like to thank all the station operators who conducted the observations, ESOC for their collaboration in planning the observations, and ESA's MEX project team for their support and assistance. The authors would also like to acknowledge the iSWA for the ENLIL simulations and the data from the ACE spacecraft. T. Bocanegra Bahamón acknowledges the NWO-ShAO agreement on collaboration in VLBI. The spacecraft tracking software is available at an online repository (bitbucket.org/spacevlbi/). The data presented in this paper are available at an online repository (bitbucket.org/spacevlbi/cme-monitoring).

References

Ando, H., Shiota, D., Imamura, T., Tokumaru, M., Asai, A., Isobe, H., … Nakamura, M. (2015). Internal structure of a coronal mass ejection revealed by Akatsuki radio occultation observations. *Journal of Geophysical Research: Space Physics*, *120*, 5318–5328. https://doi.org/10.1002/2015JA021076

Armstrong, J. W. (1998). Radio wave phase scintillation and precision Doppler tracking of spacecraft. *Radio Science*, *33*(6), 1727–1738.

Asmar, S. W., Armstrong, J. W., Iess, L., & Tortora, P. (2005). Spacecraft Doppler tracking: Noise budget and accuracy achievable in precision radio science observations. *Radio Science*, *40*, RS2001. https://doi.org/10.1029/2004RS003101

Beasley, A. J., & Conway, J. E. (1995). VLBI phase-referencing. In *ASP*, *82* (pp. 327).

Bird, M. K., Volland, H., Pätzold, M., Edenhofer, P., Asmar, S. W., & Brenkle, J. P. (1994). The coronal electron density distribution determined from dual-frequency-frequency ranging measurements during the 1991 solar conjunction of the Ulysses spacecraft. *The Astrophysical Journal*, *426*, 373–381.

Bird, M. K., Pätzold, M., Edenhofer, P., Asmar, S. W., & McElrath, T. P. (1996). Coronal radio sounding with Ulysses: solar wind electron density near 0.1 AU during the 1995 conjunction. *Astronomy and Astrophysics*, *316*, 441–448.

Cane, H. V., & Richardson, I. G. (2003). Interplanetary coronal mass ejections in the near-Earth solar wind during 1996–2002. *Journal of Geophysical Research*, *108*, 1156. https://doi.org/10.1029/2002JA009817

Chen, P. F. (2011). Coronal mass ejections: Models and their observational basis. *Living Reviews in Solar Physics*, *8*(1), 92.

Coles, W. A., Harmon, J. K., Lazarus, A. J., & Sullivan, J. D. (1978). Comparison of 74-MHz interplanetary scintillation and IMP 7 observations of the solar wind during 1973. *Journal of Geophysical Research*, *83*(A7), 3337–3341.

Davis, C. J., Davies, A., Lockwood, M., Rouillard, A. P., Eyles, C. J., & Harrison, R. A. (2009). Stereoscopic imaging of an Earth-impacting solar coronal mass ejection: A major milestone for the STEREO mission. *Geophysical Research Letters*, *36*, L08102. https://doi.org/10.1029/2009GL038021

Domingo, V., Fleck, B., & Poland, A. I. (1995). The SOHO mission: An overview. *Solar Physics*, *162*, 1–37.

Dorrian, G. D., Breen, A. R., Brown, D. S., Davies, J. A., Fallows, R. A., & Rouillard, A. P. (2008). Simultaneous interplanetary scintillation and heliospheric imager observations of a coronal mass ejection. *Geophysical Research Letters*, *35*, L24104. https://doi.org/10.1029/2008GL036181

Duev, D. A., Molera Calvés, G., Cimo, G., Bocanegra-Bahamon, T, Pogrebenko, S. V., & Gurvits, L. I. (2012). Spacecraft VLBI and Doppler tracking: Algorithms and implementation. *Astronomy and Astrophysics*, *541*, A43.

Duev, D. A., Cimo, S. V., Molera Calves, G., Bocanegra Bahamon, T. M., Gurvits, L. I., Kettenis, M. M., … Witasse, O. (2016). Pogrebenko Planetary Radio Interferometry and Doppler Experiment (PRIDE) technique: A test case of the Mars Express Phobos fly-by. *Astronomy and Astrophysics*, *593*, A34.

Efimov, A. I., Samoznaev, L. N., Bird, M. K., Chashei, I. V., & Plettemeier, D. (2008). Solar wind turbulence during the solar cycle deduced from Galileo coronal radio-sound experiments. *Advances in Space Research*, *42*, 117–123.

Efimov, A. I., Armand, N. A., Lukanina, L. A., Samoznaev, L. N., Chashei, I. V., & Bird, M. K. (2009). Investigation of coronal mass ejections by the two-position radio sounding method. *Geomagnetism and Aeronomy*, *49*(8), 1165–1169.

Futaana, Y., Barabash, S., Yamauchi, M., McKenna-Lawlor, S., Lundin, R., Luhmann, J. G., … Bochsler, P. (2008). Mars Express and Venus Express multi-point observations of geoeffective solar flare events in December 2006. *Planetary and Space Science*, *56*, 873–880.

Gosling, J. T. (1990). Coronal mass ejections and magnetic flux ropes in interplanetary space. In E. R. Priest, L. C. Lee, & C. T. Russel (Eds.), *Physics of magnetic flux ropes, Geophysical Monograph* (Vol. 58, pp. 343–364). Washington, DC: American Geophysical Union.

Jackson, B. V., Hick, P. L., Kojima, M., & Yokobe, A. (1998). Heliospheric tomography using interplanetary scintillation observations: 1. Combined Nagoya and Cambridge data. *Journal of Geophysical Research*, *103*(A6), 12,049–12,067. https://doi.org/10.1029/97JA02528

Jones, R. A., Breen, A. R., Fallows, R. A., Canals, A., Bisi, M. M., & Lawrence, G. (2007). Interaction between coronal mass ejections and the solar wind. *Journal of Geophysical Research*, *112*, A08107. https://doi.org/10.1029/2006JA011875

Hardwick, S. A., Bisi, M. M., Davies, J. A., Breen, A. R., Fallows, R. A., Harrison, R. A., & Davis, C. J. (2013). Observations of rapid velocity variations in the slow solar wind. *Solar Physics*, *285*, 111–126. https://doi.org/10.1007/s11207-013-0223-x

Hewish, A., Scott, P. F., & Wills, D. (1964). Interplanetary scintillation of small diameter radio sources. *Nature*, *203*, 1214–1217. https://doi.org/10.1038/2031214a0

Kaiser, M. L., Kucera, T. A., Davila, J. M., St. Cyr, O. C., Guhathakurta, M., & Christian, E. (2008). The STEREO mission: An introduction. *Space Science Reviews*, *136*, 5–16.

Karl, J., Pätzold, M., & Bird, M. K. (1997). Coronal radio sounding: Non-Gaussian turbulence in the source regions of the solar wind. *Geophysical Research Letters*, *24*, 2881–2884.

Kay, C., dos Santos, L. F. G., & Opher, M. (2015). Constraining the mass and the non-radial drag coefficient of a solar coronal mass ejection. *The Astrophysical Journal Letters*, *801*, L21.

Kim, T. K., Pogorelov, N. V., Borovikov, S. N., Jackson, B. V., Yu, H.-S., & Tokumaru, M. (2014). MHD heliosphere with boundary conditions from a tomographic reconstruction using interplanetary scintillation data. *Journal of Geophysical Research: Space Physics*, *119*, 7981–7997. https://doi.org/10.1002/2013JA019755

Kojima, K., Tokumaru, M., Watanabe, H., Yokobe, A., Asai, K., Jackson, B. V., & Hick, P. L. (1998). Heliospheric tomography using interplanetary scintillation observations: 2. Latitude and heliocentric distance dependence of solar wind structure at 0.1–1 AU. *Journal of Geophysical Research*, *103*(A2), 1981–1989. https://doi.org/10.1029/97JA02162

Kolmogorov, A. N. (1991). Turbulence and stochastic processes: Kolmogorov's ideas 50 years on the local structure of turbulence in incompressible viscous fluid for very large Reynolds numbers. *Proceedings of the Royal Society, London, A*, *434*, 9–13. https://doi.org/10.1098/rspa.1991.0075

Kubicka, M., Möstl, C., Amerstorfer, T., Boakes, P. D., Feng, L., Eastwood, J. P., & Törmänen, O. (2016). Prediction of geomagnetic storm strength from inner heliospheric in situ observations. *The Astrophysical Journal*, *833*, 255. https://doi.org/10.3847/1538-4357/833/2/255

Liu, Y., Luhmann, J. G., Muller-Mellin, R., Choeder, P. C., Wang, L., Lin, R. P., … Sauvaud, J. A. (2008). A comprehensive view of the 2006 December 13 CME: From the Sun to interplanetary space. *The Astrophysical Journal*, *689*, 563–571.

Molera Calvés, G. (2012). Radio spectroscopy and space science with VLBI radio telescopes for solar system research (PhD dissertation), Aalto University. Pub. No. 42/2012.

Molera Calvés, G., Pogrebenko, S. V., Cimò, G., Duev, D. A., Bocanegra-Bahamón, T. M., Wagner, J. F., … Hao, L. F. (2014). Observations and analysis of phase scintillation of spacecraft signal on the interplanetary plasma. *Astronomy and Astrophysics*, *564*(A4), 7.

Pätzold, M., Hahn, M., Tellmann, S., Häusler, B., Bird, M. K., Tyler, L., … Tsurutani, B. T. (2012). Coronal density structures and CMEs: Superior solar conjunctions of Mars express, Venus express, and Rosetta: 2004, 2006 and 2008. *Solar Physics*, *279*, 127–152.

Sokól, J. M., Bzowski, M., Tokumaru, M., Fujiki, K., & McComas, D. J. (2013). Heliolatitude and time variations of solar wind structure from in situ measurements and interplanetary scintillation observations. *Solar Physics*, *285*, 167–200. https://doi.org/10.1007/s11207-012-9993-9

Woo, R., Armstrong, J. W., & Gazis, P. R. (1995). Doppler scintillation measurements of the heliospheric current sheet and coronal streamers close to the Sun. In *Proceedings of the 28th ESLAB symposium* (pp. 223). Friedrichshafen, Germany.

Woo, R., Yang, F.-C., Yip, K. W., & Kendall, W. B. (1976). Measurements of large-scale density fluctuations in the solar wind using dual-frequency phase scintillations. *The Astrophysical Journal*, *210*, 568–574.

You, X. P., Coles, W. A., Hobbs, G. B., & Manchester, R. N. (2012). Measurement of the electron density and magnetic field of the solar wind using millisecond pulsars. *Monthly Notices of the Royal Astronomical Society*, *422*, 1160–1165.